

Effect of footing shape on penetration in sand overlying clay

1 Pan Hu PhD

Research Associate, Centre for Offshore Foundation Systems and ARC Centre of Excellence for Geotechnical Science and Engineering, The University of Western Australia, Crawley, Australia

2 Sam A. Stanier PhD

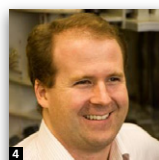
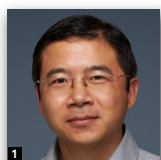
Research Fellow, Centre for Offshore Foundation Systems and ARC Centre of Excellence for Geotechnical Science and Engineering, The University of Western Australia, Crawley, Australia

3 Dong Wang PhD

Research Associate Professor, Centre for Offshore Foundation Systems and ARC Centre of Excellence for Geotechnical Science and Engineering, The University of Western Australia, Crawley, Australia

4 Mark J. Cassidy PhD

Professor and ARC Laureate Fellow, Centre for Offshore Foundation Systems and ARC Centre of Excellence for Geotechnical Science and Engineering, The University of Western Australia, Crawley, Australia



This paper reports on a series of centrifuge model tests investigating the effect of shape on the penetration resistance of spudcan and conical footings on sand overlying clay. The effect of footing shape and geometry on single-layer soil has been studied intensely. However, there is still limited understanding for conical footings on sand over clay. In the present study, digital images were captured during penetration of various shapes of half-footing held against a transparent window of a strongbox. The images were then analysed using particle image velocimetry techniques. Experimental evidence has shown that, irrespective of the conical angle of the underside within the range of 7–21°, when the footing penetrates through sand into an underlying clay layer: (a) accumulated radial and deviatoric shear strains along the future failure surface counteract each other, resulting in similar peak resistance in the sand layer and (b) a trapped sand plug of constant height is pushed into the underlying clay layer. These observations serve to justify the previously proposed methods for predicting the full penetration resistance profile on sand overlying clay, which is required to predict the potential for, and severity of, punch-through failure.

Notation

c_v	coefficient of consolidation
D	diameter of the spudcan
D_F	distribution factor
d	penetration depth
d_{peak}	spudcan depth at peak penetration resistance
E^*	parameter to simplify the algebra
H_{plug}	sand plug height
H_s	sand thickness
I_D	relative density
I_R	dilatancy indicator in degrees
k	strength gradient of clay
N_c	bearing capacity factor
$N_{c, \text{deep}}$	deep bearing capacity factor
N_{co}	bearing capacity factor of clay at base level of a circular foundation

$N_{T\text{-bar}}$	intermediate roughness factor of T-bar
Q	natural logarithm of the grain crushing strength expressed in kilopascals
q	penetration resistance
q_{clay}	penetration resistance in the clay layer
q_{peak}	peak penetration resistance
$q_{\text{peak, calculated}}$	calculated peak penetration resistance
$q_{\text{peak, experiment}}$	measured peak penetration resistance
q_0	effective overburden pressure
r	radius
s_{um}	shear strength of clay at sand–clay interface
s_{u0}	clay shear strength at the lowest level of the spudcan maximum cross-sectional area
u	radial displacement
V	dimensionless velocity
v	penetration rate of footing

γ_{tz}	engineering shear strain
γ'_c	effective unit weight of clay
γ'_s	effective unit weight of sand
ε_{dev}	deviatoric shear strain
ε_r	radial strain
ε_z	normal strain
ε_θ	circumferential strain
ϕ_{cv}	critical state friction angle of sand
ϕ'	friction angle of sand
ϕ^*	reduced friction angle due to non-associated flow rule
ψ	dilation angle of sand

1. Introduction

Mobile jack-up units are widely used for offshore drilling in water depths of up to ~120 m. Modern jack-up rigs are typically supported by three independent truss legs, with each attached to a large inverted conical footing called a spudcan. Spudcan designs change depending on the manufacturer, with conical angles usually ranging from 0° to 20°, although some can be even sharper up to 40° (Dean, 2010; Menzies and Roper, 2008).

When considering the installation of jack-up foundations, it is necessary to predict their bearing capacity with depth to assess the potential for ‘punch-through’ type failure. Punch through occurs when the bearing pressure suddenly reduces following failure of a stiff top layer overlying a softer layer, such as sand overlying clay. This type of failure has been modelled extensively in the centrifuge (Craig and Chua, 1990; Hu *et al.*, 2014a; Lee *et al.*, 2013a; Teh *et al.*, 2008, 2010). Apart from the methods recommended in the ISO (2012) guideline, prediction methods for estimating ‘punch through’ have been developed based on these experiments (Hu *et al.*, 2014a, 2014b; Lee *et al.*, 2013b) by estimating the peak resistance in the sand layer, q_{peak} , and the penetration resistance in the underlying clay layer, q_{clay} . As it has been demonstrated in Hu *et al.* (2014a) and Lee *et al.* (2013b) that the ISO methods are poor at predicting q_{peak} , these newly developed methods are potentially useful – once validated – in helping jack-up operators to quantify the risk of ‘punch-through’ based on the spudcan geometry and seabed conditions (Osborne *et al.*, 2009). However, the sensitivity of footing geometry on the governing deformation mechanisms during penetration of a footing through sand overlying clay has not been sufficiently investigated for such methods to be used for different spudcan shapes with confidence.

The primary focus of this paper is to address this shortcoming experimentally and assess the validity of the previously proposed approaches for a range of spudcan geometries and to

highlight the mechanisms and features that demonstrate why the more sophisticated models work well in comparison.

2. Background to analytical models used in paper

The peak penetration resistance, q_{peak} , in the sand layer and the resistance in the clay layer, q_{clay} are two critical components in approximating the full penetration resistance profile analytically. Through a series of spudcan (for a base conical angle of 13°) and flat footing penetration tests on very dense sand (relative density $I_D=92\%$) overlying clay, a failure stress-dependent model was proposed by Lee *et al.* (2013b) to calculate q_{peak} . This model assumes an inverted and truncated cone of sand with an inclination angle equal to the dilation angle is pushed down into the underlying clay. Hence, the value of q_{peak} consists of the frictional resistance from the shearing sand and the bearing resistance from the underlying clay. The model was modified by Hu *et al.* (2014a) (Figure 1) to account for mobilisation embedment depth and validated experimentally for medium to very dense sand, again for a spudcan geometry with a base conical angle of 13°, resulting in the following expression

$$1. \quad q_{peak} = (N_{c0}s_{um} + q_0 + 0.12\gamma'_s H_s) \times \left(1 + \frac{1.76H_s}{D} \tan \psi\right)^{E^*} + \frac{\gamma'_s D}{2 \tan \psi (E^* + 1)} \times \left[1 - \left(1 - \frac{1.76H_s}{D} E^* \tan \psi\right) \left(1 + \frac{1.76H_s}{D} \tan \psi\right)^{E^*}\right]$$

where N_{c0} is the bearing capacity factor for clay at the base of a circular foundation, which is obtained using the lower bound solutions proposed by Houlsby and Martin (2003); s_{um} is the undrained shear strength of clay at the sand–clay interface; q_0 is the effective overburden pressure at the depth of the foundation; γ'_s is the effective unit weight of sand; H_s is the initial sand layer thickness; D is the spudcan diameter; and ψ is the dilation angle of sand. Lastly, E^* is a parameter to simplify the algebra

$$2. \quad E^* = 2 \left[1 + D_F \left(\frac{\tan \phi^*}{\tan \psi} - 1\right)\right]$$

where D_F is a distribution factor and ϕ^* is a reduced friction angle caused by non-associated flow rule that can be expressed as (Drescher and Detournay, 1993)

$$3. \quad \tan \phi^* = \frac{\sin \phi' \cos \psi}{1 - \sin \phi' \sin \psi}$$

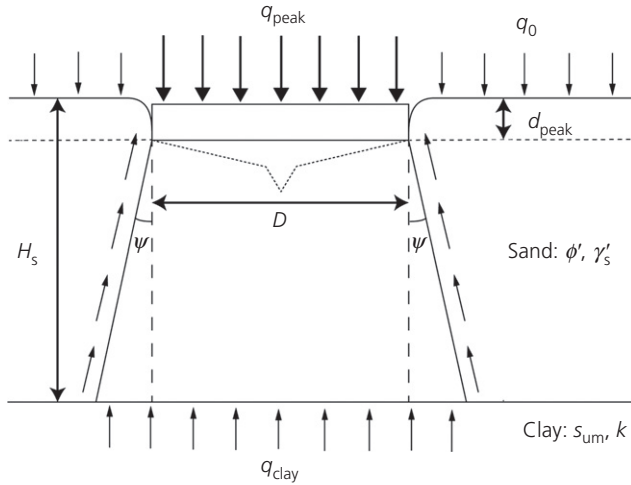


Figure 1. Modified failure stress-dependent mechanism accounting for embedment depth attained during mobilisation of q_{peak} (after Hu *et al.*, 2014a)

where ϕ' is the friction angle of sand. The expression for q_{peak} was derived from the integration of the vertical force equilibrium equation on an infinitesimal element, in which the distribution factor D_F is an empirical factor intended to relate the normal effective stress on the slip surface to the average vertical effective stress on the infinitesimal element in the sand layer beneath the footing. The distribution factor is the only empirical parameter in these models and was found to depend only on the sand thickness ratio H_s/D , which was expressed originally by way of a pair of linear equations for spudcan (13° conical underside) and flat footings, respectively (Lee *et al.*, 2013b). Accounting for mobilisation depth and further experimental evidence after Hu *et al.* (2014a), the distribution factor was modified, and for spudcans it was recommended as

$$4. \quad D_F = 0.642 \left(\frac{H_s}{D} \right)^{-0.576} \quad \text{as} \quad 0.16 \leq \frac{H_s}{D} \leq 1.0$$

By assuming the same modified mechanism and based on the very dense sand tests of Lee *et al.* (2013a), a similar power relationship for a flat footing can be found as

$$5. \quad D_F = 0.623 \left(\frac{H_s}{D} \right)^{-0.174} \quad \text{as} \quad 0.21 \leq \frac{H_s}{D} \leq 1.12$$

These power relations give a closer fit for a larger range of geometries and material properties than the linear fits of Lee *et al.* (2013b). The inequalities presented alongside the D_F relations represent the geometric range of sand layer thickness to spudcan diameter over which the fits were calculated.

When the spudcan penetrates through the sand into the clay, a sand plug is trapped underneath the spudcan and Hu *et al.* (2014b) showed that the penetration resistance in the clay layer could be adequately expressed as

$$6. \quad \begin{aligned} q_{\text{clay}} &= N_c s_{u0} + H_{\text{plug}} \gamma'_c \\ &= N_c s_{u0} + 0.9 H_s \gamma'_c \quad \left(0.16 \leq \frac{H_s}{D} \leq 1 \right) \end{aligned}$$

where N_c is the bearing capacity factor in the clay layer; s_{u0} is the soil shear strength at the load reference point (taken as the lowest level of the maximum cross-section of the footing); H_{plug} is the sand plug height; and γ'_c is the effective unit weight of clay. The first term is the bearing capacity for a composite foundation of spudcan and trapped sand plug in weightless soil, while the second term accounts for buoyancy of sand plug surrounded by clay. Craig and Chua (1990) observed that the trapped sand plug had a height equal to H_s through an examination of cross-sections of spent centrifuge samples. By conducting particle image velocimetry (PIV) analysis on a half-spudcan model, Teh *et al.* (2008) also reported that the trapped sand plug height was $\sim 1H_s$ and the upper portion of the trapped sand resembled a cylinder, while the lower part was somewhat irregularly shaped. A value of $0.9H_s$ was recommended in Teh (2007) for spudcan with 13° underside. On the basis of centrifuge tests of medium dense sand ($I_D = 43\%$) overlying clay and complementary parametric studies on loose and medium dense sand, N_c was back-calculated by Hu *et al.* (2014b) and normalised by the deep bearing capacity factor, $N_{c, \text{deep}}$ (taken as the value of N_c at $1D$ depth below the sand–clay interface). By incorporating the combined geometry of the spudcan and sand plug, an equation for N_c was proposed based on the best fit of $N_{c, \text{deep}}$

$$7. \quad N_c = 15 \frac{H_s}{D} + 9 \left(0.16 \leq \frac{H_s}{D} \leq 1 \right)$$

All these design methodologies were formulated based on centrifuge tests performed using a spudcan footing of 13° base conical angle. However, spudcan footings used on jack-up rigs do not always have the same geometry as the conical angle of the underside often varies, with some example shapes used on offshore rigs illustrated in Cassidy *et al.* (2009) and Dean (2010). The aims of this paper are to investigate the impact of varying the conical angle of the underside of a footing on the validity of Equations 1–7 by the following.

- Modelling the effect of angle of a conical footing on the peak resistance in medium dense sand overlying clay in a centrifuge.
- Observing the failure mechanisms during all stages of punch through using PIV techniques, revealing the effect of footing shape on: (a) the peak resistance; (b) the trapped

sand plug height; and (c) the bearing capacity mechanisms in the underlying clay layer.

- Assessing the performance of the models given by Equations 1–7 for estimating the ‘punch-through’ risk.

3. Experimental methodology

A series of half-footing penetration tests were performed in the drum centrifuge at the University of Western Australia (UWA) with the soil flow mechanisms around the footings being observed using the PIV apparatus developed by Stanier and White (2013). Figure 2(a) shows a general view of the testing apparatus. Images recorded during the tests were then analysed to reveal the deformation mechanisms (White *et al.*, 2003).

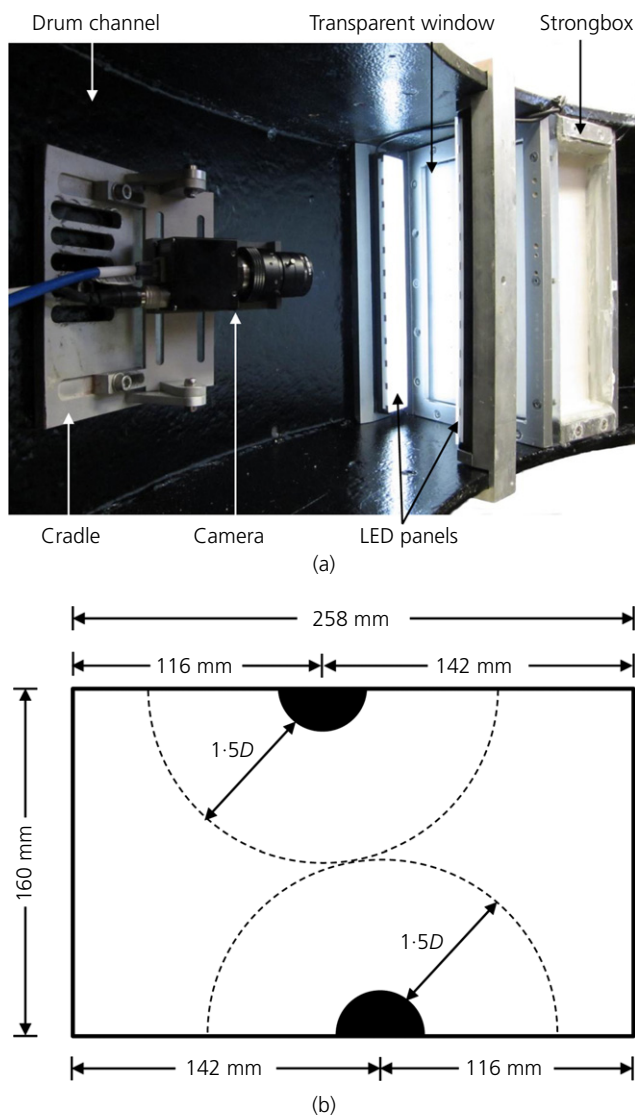


Figure 2. Testing configurations: (a) testing apparatus and (b) top view of the strongbox

The testing program was designed to span a large range of normalised sand thickness, H_s/D , thus encompassing the range of practical interest to jack-up operators. The angles of the conical footing models were in the range commonly found offshore of 0–21°.

3.1 Experimental set-up

The experimental set-up consisted of a machine vision camera with an image resolution of ~5 million pixels mounted in front of the viewing window and aligned so as to minimise the non-coplanarity of the transparent window and camera. The soil samples were prepared in strongboxes with internal dimensions of 258 mm length × 160 mm width × 160 mm depth, with a transparent sidewall providing an exposed cross-section viewing area of 258 mm × 160 mm (Figure 2(b)). The strongbox was fitted into the ring channel of the drum centrifuge with its exposed plane parallel to the centre of centrifuge rotation. A pair of light emitting diode panels with diffusing filters, positioned along the top and bottom of the strongbox, uniformly illuminated the exposed face of the samples.

Five half-footing models (Figure 3), including four simple conical footings and one with an additional spigot, were tested and are referred to as models C0, C7, C14, C21 and S13, respectively. Prefix ‘C’ refers to the cone-shaped footings and ‘S’ refers to the model with the additional spigot. The accompanying number refers to the angle of the base conical section. All footings shared a similar upper conical angle of 13°. For straightforward comparison to previously published data, model S13 had the same geometry as that used by Hu *et al.* (2014a), Lee *et al.* (2013a) and Teh *et al.* (2008, 2010). All models were semi-circular in shape, with diameter D of 40 mm. The diameter of the footing was chosen so as to be sufficiently large to allow reasonably detailed images of the soil flow patterns to be captured while avoiding boundary effects from the edge of the strongbox. To take full advantage of the testing area, two tests were conducted on opposite sides of each strongbox, as illustrated in Figure 2(b). Craig and Chua (1990) and Hossain *et al.* (2006) reported that interference between tests during footing penetration was minimal with a free-space width of 1.5 D between tests. The minimum distance between the two footing test locations in each strongbox was thus set as 3 D . It has also been validated in Hu (2015) to cause no boundary effect through large deformation finite-element analysis using the coupled Eulerian–Lagrangian approach in commercial package Abaqus. To achieve proper sealing and prevent soil ingress between the window and back plate of the footing model, closed-cell foam was attached to the flat surface of the footing and lightly greased before being pressed against the inner side of the transparent window by the actuator. The footing load was measured using an S-shaped load cell; oriented so as to be affected minimally

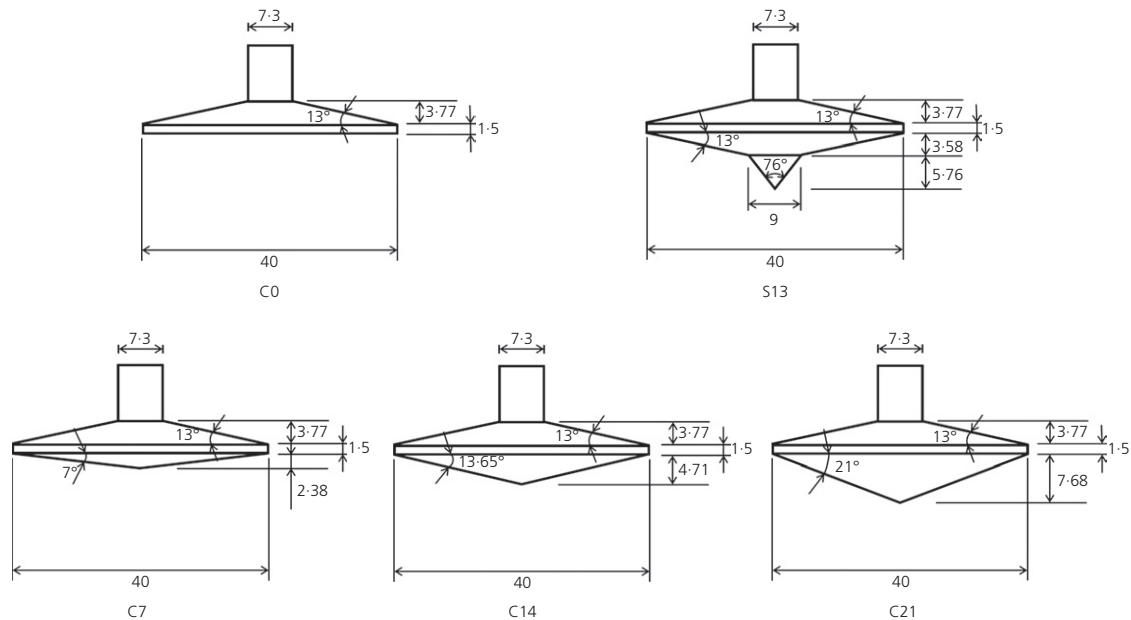


Figure 3. Dimensions of model footings used in centrifuge test
(all measurements in mm)

Soil	Property	Symbol	Value
Superfine silica sand	Specific gravity	G_s	2.65
	Average effective particle size	d_{50}	0.19 mm
	Maximum void ratio	e_{max}	0.75
	Minimum void ratio	e_{min}	0.45
	Critical state friction angle	ϕ_{cv}	31°
UWA kaolin clay	Liquid limit	LL	0.61
	Plastic limit	PL	0.27
	Specific gravity	G_s	2.6
	Angle of internal friction	ϕ'	23°
	Coefficient of consolidation (at 20 kPa)	C_v	~2 m ² /year

Table 1. Engineering properties of superfine silica sand and UWA kaolin clay

by the bending moments generated within the shaft of the spudcan. Buoyancy and friction between the footing and window were measured in repeat tests in strongboxes containing only water. These effects were then subtracted from the response measured for the models containing soil during the analysis process. The efficacy of such PIV model-based measurements has been manifested in Stanier *et al.* (2014).

3.2 Sample preparation

Commercially available superfine silica sand and kaolin clay were used as the upper sand and lower clay layer, respectively.

Both have been used extensively in previous centrifuge model studies at UWA, with their behaviour well documented (Acosta-Martinez and Gourvenec, 2006; Cheong, 2002). The material properties of the sand and clay are provided in Table 1.

A bed of clay was formed in each strongbox by pouring kaolin slurry (mixed at 120% water content under vacuum) in-flight at 40g followed by consolidation at 300g. With the clay layer pre-consolidated, dry superfine silica sand was air pluviated into each chamber at 1g using an electrically controlled

bar-type sand hopper. The densities of the sand layers formed were determined from measurements of the total added sand weight and the volume the layer occupied in the strongbox. The average relative density, I_D , was 74% while the standard deviation was 7%, indicating excellent uniformity between strongboxes. This gives the sand layer an effective unit weight γ'_s of 10.6 kN/m³ on average. The dry sand bed was partially saturated prior to replacement of the sample in the drum centrifuge channel to provide sufficient capillarity in the sand layer so that the sample did not collapse during remounting.

The final preparation stage prior to testing was to ensure optimal precision of the PIV measurements by applying artificial seeding to the exposed plane of each model. Black and green coloured artificial seeding was evenly sprinkled onto the exposed sand and clay layers, respectively, enhancing the visual texture of the sand and clay and allowing easy detection of movement. The optimal densities of seeding on the sand and clay layers were defined by following the procedure proposed by Stanier and White (2013). The transparent window was then reinstalled before the strongbox was carefully slotted into the centrifuge channel. The sand layers were back saturated using water during ramping-up and the sample was then subjected to an acceleration level of 300g and allowed to further consolidate. All tests were carried out at an acceleration of 200g. This resulted in a gradient of the shear strength within the clay layer that allowed the full punch-through process to be modelled within the confines of the strongbox.

3.3 Testing procedure

Once the soil sample was fully consolidated, the penetration test commenced and images were recorded simultaneously. The footing penetration location was positioned close to the

centre of the strongbox window, giving a clearance of at least 2.4D between the footing edge and the sidewall of the strongbox. This clearance was deemed sufficient in view of the fact that the majority of soil flow induced by the spudcan penetration in the sand overlying clay occurs within a distance of $\sim 1D$ from the spudcan edge (Teh *et al.*, 2008). The footing penetration process was displacement controlled at a rate of $v = 0.19$ mm/s. This displacement rate ensured that the dimensionless velocity, $V = vD/c_v$, was < 0.01 for the sand layer and ~ 120 in the clay layer, ensuring a drained sand response and undrained clay response (Cassidy, 2012; Chung *et al.*, 2006), where c_v is the coefficient of consolidation. Images were captured continuously in-flight at 5 frames/sec, which equates to an image for every 0.038 mm of (model scale) displacement, providing excellent resolution for visualisation of the failure mechanism. The soil displacement trajectories were computed from the images recorded using the PIV technique (e.g. White *et al.*, 2003). The analysis process included application of close-range photogrammetric corrections to convert the image space coordinates into object space coordinates, accounting for image distortions.

Two different sand thicknesses were prepared within each soil sample. The thicker sand layer was tested first, and then the channel was brought to a standstill so that sand could be scraped from the surface until the desired sand thickness was achieved ready for the next test. Actual sand layer thicknesses were measured using the same close range photogrammetry techniques for correcting the displacement measurements. On each occasion, the sample was left to reconsolidate with the new sand thickness before commencement of the penetration test. Table 2 provides a summary of the 11 tests performed, alongside the measured sand layer heights.

Experimental details									Results			
Test identifier	H_s : m	D : m	H_s/D	Conical angle: deg	I_D : %	s_{um} : kPa	k : kPa/m	D_F	q_{peak} : kPa	ϕ' : deg	ψ : deg	$N_{c, deep}$
H7C7	6.89	8	0.86	7	74	21.86	2.09	0.73	702.82	35.2	5.3	20.97
H7C14	7.11	8	0.89	13.65	74	22.24	2.11	0.75	758.95	35.1	5.2	—
H7C21	7.25	8	0.91	21	74	22.22	2.09	0.71	740.25	35.1	5.1	—
H5C0	4.91	8	0.61	0	74	19.29	2.08	0.61	368.11	36.4	6.7	15.51
H5C7	5.09	8	0.64	7	74	16.66	1.80	0.83	436.74	36.0	6.3	16.48
H5S13	5.13	8	0.64	13	74	19.58	2.08	0.81	487.82	35.8	6.0	—
H5C14	5.41	8	0.68	13.65	74	20.72	2.13	0.75	504.69	35.6	5.8	—
H5C21	5.25	8	0.66	21	74	20.55	2.13	0.72	456.93	35.7	5.8	15.27
H3C7	3.05	8	0.38	7	74	11.34	1.51	1.20	246.36	37.3	7.8	14.20
H3C14	3.03	8	0.38	13.65	74	11.31	1.51	1.16	237.28	37.3	7.9	16.65
H3C21	3.18	8	0.40	21	74	13.93	1.83	0.99	261.95	36.9	7.4	15.10

Table 2. Summary of half-footing penetration tests and results

4. Penetration resistance profiles

After correction to account for buoyancy and interface friction between the footing and the transparent window, the remaining force was divided by the cross-sectional area at the load reference point to obtain the penetration resistance, q . The penetration depth, d , is defined as zero when the lowest level of the spudcan largest cross-section touches the soil. The undrained shear strength profile of the underlying clay was estimated using miniature T-bar tests conducted after removal of the upper sand layer, assuming an intermediate roughness $N_{T\text{-bar}}$ factor of 10.5 (Stewart and Randolph, 1991). This avoided the problem of sand becoming trapped beneath the T-bar during penetration through the sand layer, which causes

an overestimation of the shear strength of clay. Strength profiles were linear with increasing strength with depth, with the strength at the sand–clay interface and strength gradient, k , for all samples summarised in Table 2.

The response measured for all tests with similar H_s/D ratios are presented in Figure 4 to a final penetration depth of $1D$ from the base of the strongbox, beyond which boundary effects were observed (as modelled numerically by Ullah and Hu, 2012). For tests H7C21, H7C14, H5C21 and H5S13, the penetration resistance in the clay layer for depths beyond $1D$ from the sand–clay interface appeared odd due to sudden reductions in the magnitudes of penetration resistances. Assessment of the

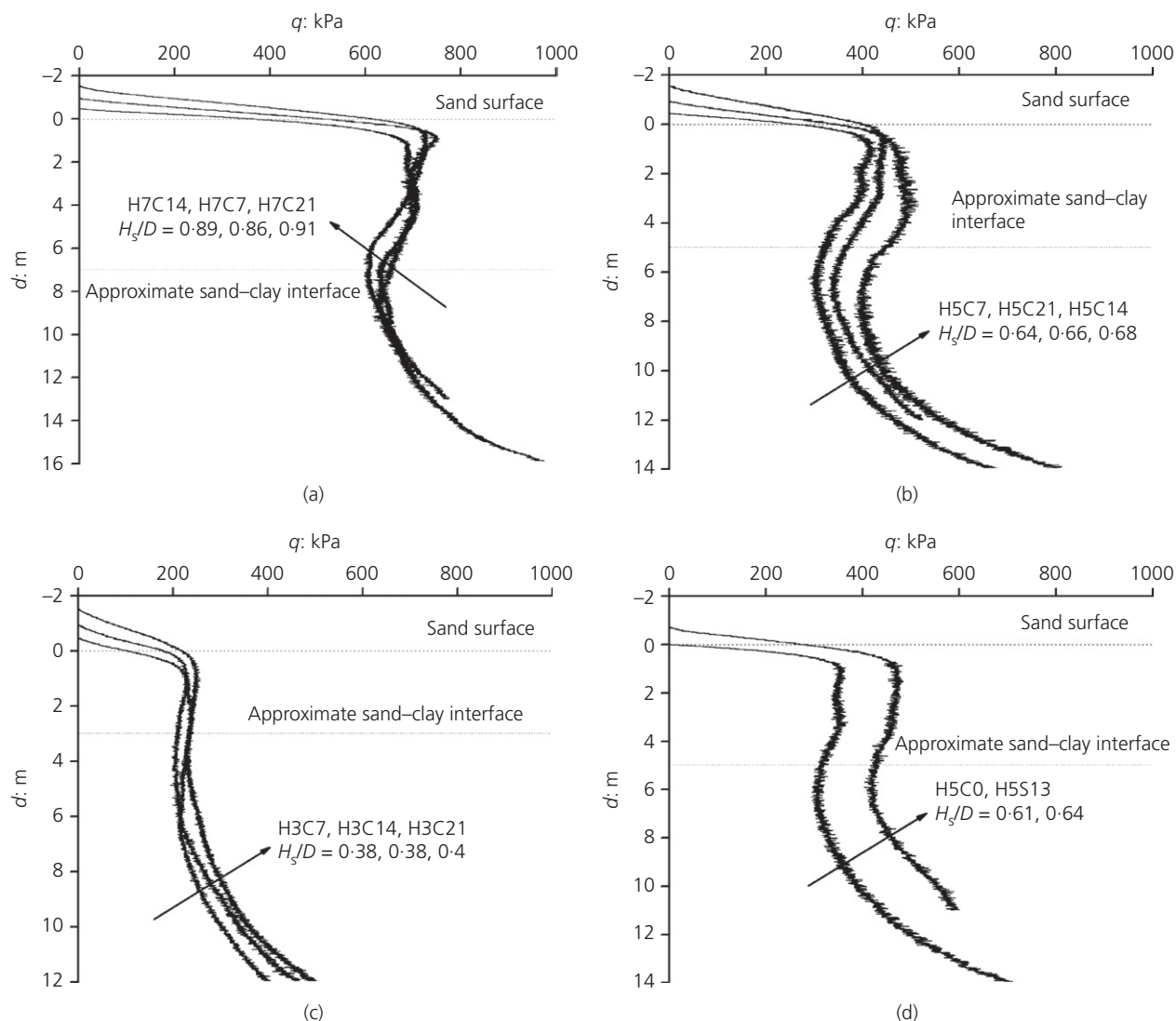


Figure 4. Full penetration resistance profiles from PIV tests (dimensions given in prototype scale)

PIV images showed this was due to an apparent loss of sand plug volume that may have been caused by the footing becoming misaligned with the transparent window at such large depths, thus the responses beyond these depths were ignored.

In general, the penetration resistance began to increase when the tip of the conical footing penetrated into the sand and increased rapidly due to the increasing contact area up until the q_{peak} was mobilised. Subsequent penetration led to a nearly constant or small reduction in resistance with the minimum penetration resistance observed close to the original depth of the sand–clay interface. Beyond this point, the penetration resistance increased gradually with penetration depth due to the increasing clay strength with depth. The measured penetration resistance profiles in terms of footings with different shapes indicate the following.

- The q_{peak} for the flat footing (C0) was lower than tests performed with a cone-shaped footing (C7, C14, C21) for a similar H_s/D ratio. This has implications on the form of design equations for predicting q_{peak} as will be demonstrated later.
- The majority of the tests exhibited near-constant penetration resistance following q_{peak} before gradually increasing penetration resistance with depth. Potential prototype depths of penetration before increasing capacity were ~10 m, indicating a significant punch-through risk.

5. Peak resistance in sand

5.1 Distribution factors for varying spudcan geometries

Assuming the failure stress-dependent failure mechanism of Hu *et al.* (2014a), the values of D_F for all the penetration tests conducted were back calculated and are plotted in Figure 5(a) alongside back-calculated values for other recent centrifuge tests on fully circular model spudcans (Hu *et al.*, 2014a; Lee *et al.*, 2013b).

Lee *et al.* (2013a) observed that a spudcan has a higher D_F value than an equivalent flat footing for the same H_s/D ratio and suggested that the reason may be that higher radial stress and thus resistance along the assumed slip surface in the sand are invoked by the conical underside of the spudcan. Extrapolating from this, it might also be plausible to assume that larger conical angles lead to larger D_F values. However, Figure 5(a) shows this not to be the case since all of the footing tests with conical angles between 7° and 21° exhibit similar D_F values, irrespective of the angle of the conical underside.

Using the expressions for D_F given by Equation 4 for the footings with conical angles between 7° and 21° and Equation 5

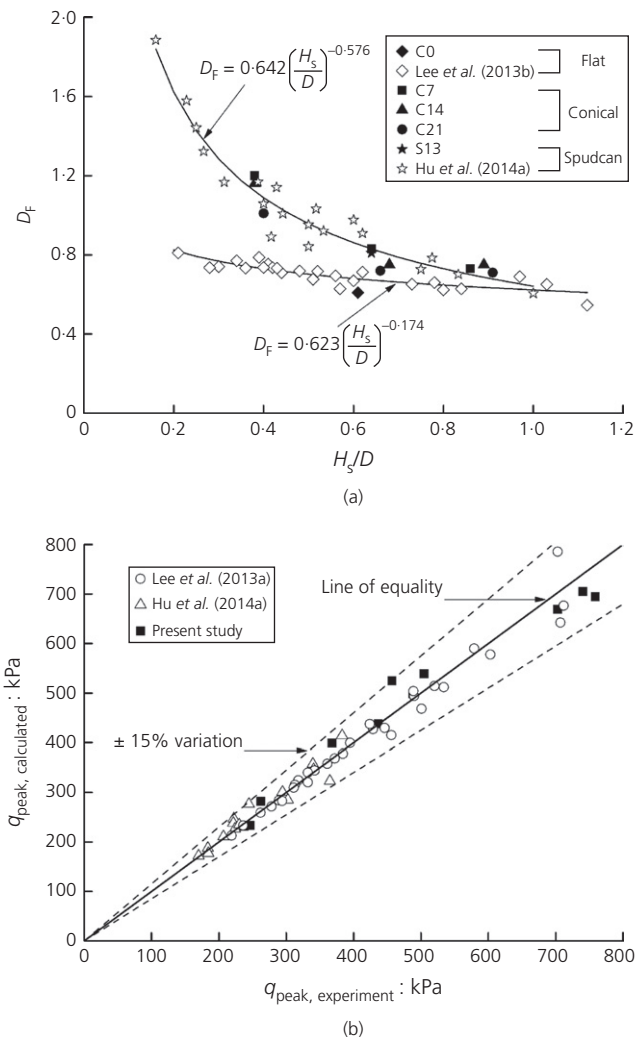


Figure 5. (a) Back-calculated distribution factors, D_F , from half-footing PIV tests compared with previous centrifuge tests (note: solid markers represent experiments performed in the present study while hollow markers represent previous experiments) and (b) comparison of the measured q_{peak} and that predicted using the modified failure stress-dependent model of Hu *et al.* (2014a)

for flat footings, the peak resistances predicted by the analytical model of Hu *et al.* (2014a) compared with published experimental measurements are plotted in Figure 5(b). Compared with the predictions from the analytical model of Hu *et al.* (2014a), all the experimental data are located within bounds of $\pm 15\%$. This indicates that the results of the half model tests described in this paper are consistent with their conventional full model equivalents, thus the influence of boundary effects caused by soil and foundation contact with the transparent window was deemed negligible.

Figure 6 compares the accumulated radial and deviatoric shear strains generated by penetration of two footings with differing conical angles up to the point at which peak resistance was mobilised. The soil displacements were measured using GeoPIV, taking a patch size of 50 pixels and spacing of 10 pixels. The reference image was updated periodically to preserve the correlation in the PIV computations, allowing large deformations to be tracked. The strains were then obtained from the displacement fields using a finite-strain formulation after White and Bolton (2004) and accumulated throughout the analyses. The radial strain was calculated as

$$8. \quad \epsilon_r = \frac{\partial u}{\partial r}$$

where u is the radial displacement and r is the radius. While the deviatoric shear strain was taken as

$$9. \quad \epsilon_{dev} = \sqrt{(\epsilon_r - \epsilon_z)^2 + (\epsilon_r - \epsilon_\theta)^2 + (\epsilon_z - \epsilon_\theta)^2 + 0.5\gamma_{rz}^2}$$

where ϵ_z is the normal strain, ϵ_θ the circumferential strain and γ_{rz} is the engineering shear strain.

The larger conical angle clearly causes greater radial strain in the vicinity of the failure surface in the sand layer, which emanates from the outer radius of the footing. However, the increasing conical angle also causes significantly larger deviatoric shear strains to accumulate within the same region, which causes strain softening of the sand reducing its mobilised friction angle.

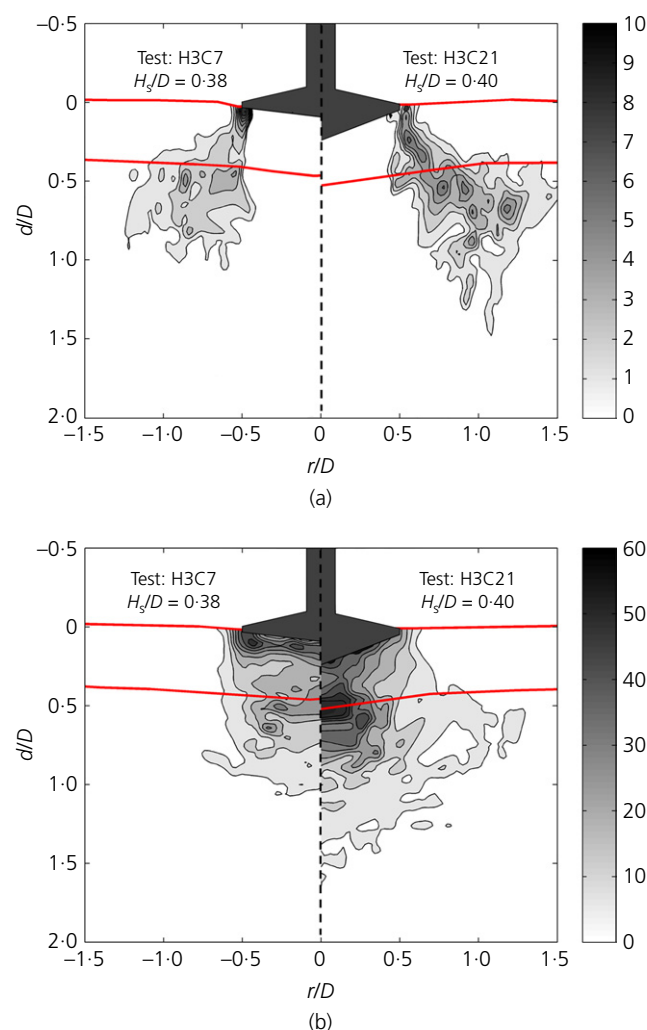


Figure 6. Accumulated (a) radial and (b) deviatoric shear strain distribution (%) for tests H3C7 and H3C21

Figure 7 plots the average accumulated radial and deviatoric shear strains measured within $0.05D$ of the inclined failure surface in the sand layer assumed in the failure stress-dependent model of Hu *et al.* (2014a) against the conical angle of the underside of the footings. Strain measurements were averaged within $0.05D$ of the failure surface to provide an estimate of the average strain that occur within the shear band formed at the assumed failure surface. An averaging distance of $0.05D$ implies a shear band thickness of $0.05D$ or ten times the d_{50} of the sand particles, which is the size of a 'homogeneously heterogeneous' shear zone according to Muir Wood (2012). The average is taken so as to provide an overall

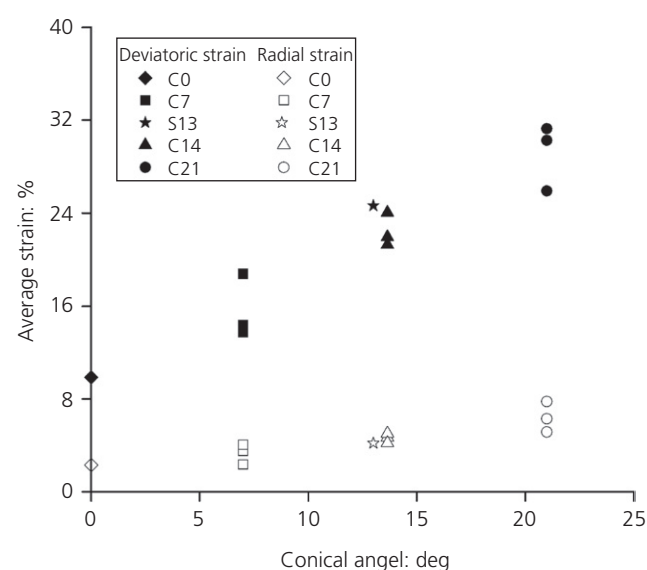


Figure 7. Average accumulated radial and deviatoric shear strains along the shear band of the soil underneath the footing

estimation of the impact of the embedment of the conical underside of the footing. The range in the accumulated strains (both radial and deviatoric shear) for a given conical angle in Figure 7 is a result of the range of H_s/D ratios tested (Table 2), which influences the calculation of the average accumulated strains. There is a clear linearly increasing trend for both strains with increasing conical angle. Thus, the increase of D_F due to higher stress is compensated for, at least partially, by the softening caused by the accumulated deviatoric shear strains. This explains why there is no systematic difference in D_F for footings with conical angles between 7° and 21° . Since the majority of the footings used in the field fall within this range (Menzies and Roper, 2008), the power relationship for D_F for spudcan footings given by Equation 4 is suitable for use in estimating q_{peak} for spudcans with geometries within the bounds investigated here.

5.2 Failure mechanism at peak resistance

Although the sand samples prepared in the centrifuge tests had similar relative density ($\sim 74\%$), the ‘average’ friction and dilation angles mobilised at peak resistance depend on the footing sizes and sand thickness. The modified failure stress-dependent model of Hu *et al.* (2014a) and Lee *et al.* (2013b), which is based on the stress–dilatancy relationships of Bolton (1986), has the ability to reflect the stress-level dependency at peak resistance. The mobilised friction and dilation angles corresponding to peak resistance for the tests in Table 2 were back calculated and are shown in Figure 8 (note: I_R is the dilatancy indicator in degrees and Q is the natural logarithm of the grain crushing strength expressed in kilopascals). The friction angle,

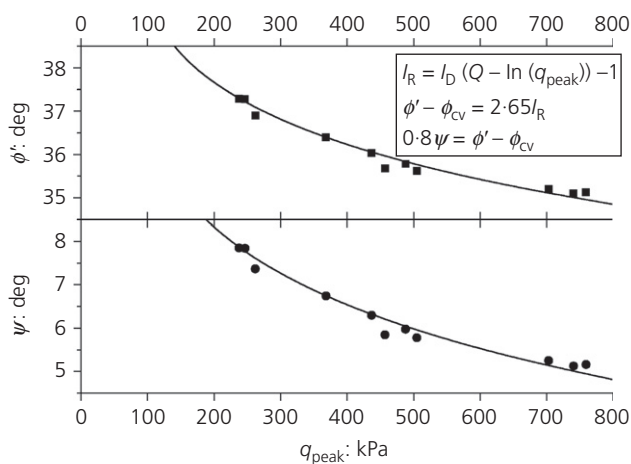


Figure 8. Back-calculated friction and dilation angles mobilised at peak resistance (line fit represents modified Bolton’s equations proposed by Hu *et al.*, (2014a) and Lee *et al.*, (2013b), as provided in the inset)

ϕ' , ranges from 37.3° to 35.1° , with the corresponding dilation angle, ψ , between 7.9° and 5.1° , with q_{peak} increasing from 237.3 to 759.0 kPa. The tendency is consistent with gradual suppression of dilatancy under increasing confining stress. This analysis provides further evidence that the incorporation of Bolton’s (1986) stress–dilatancy relationships helps the failure stress-dependent model to capture the response of sand in a realistic manner.

Figure 9 shows the normalised incremental deviatoric shear strain contours for spudcan S13 and the conical footings at peak resistance for tests with similar H_s/D . The incremental deviatoric strains are normalised by the maximum deviatoric shear strain to allow direct comparison of data from all tests in a clear manner. For each test, a series of ten images, covering a footing displacement of $\sim 0.01D$ at peak resistance was analysed. In all tests, a block of sand is pushed down to the underlying clay with inclination of the sand block at an angle similar to the back-calculated dilation angle given in Figure 8 (with the inclination angle of the failure plane – taken as equal to ψ – superimposed on the PIV images). This further validates the assumption in the modified failure stress-dependent model that the inclination angle of the failure mechanism should be taken as equal to the dilation angle of the sand at peak resistance, allowing the shape of the failure mechanism to vary depending on the sand properties. In contrast, current industry guideline (ISO, 2012) recommends the load spread method to calculate q_{peak} , where the load is assumed to spread through the upper sand layer to an imaginary footing of increased size at the sand–clay interface with an arbitrary projection angle. Furthermore, the recommended projection angles are far greater than those observed here. The PIV analyses in Figure 9 provide physical evidence that a failure stress-dependent approach is a more realistic and rational approach for predicting peak resistance than load spread method with seemingly arbitrarily fixed geometries.

6. Response in clay layer

6.1 Transition from punch-through to meta-stable penetration

Figure 10(a) presents the back-calculated normalised bearing capacity factor from test H5C0 alongside the prediction of Equation 7. Figures 10(b)–10(d) demonstrate the corresponding normalised incremental deviatoric shear strain contours at penetration depths of 0, $0.5D$ and $1.0D$ beyond the sand–clay interface, equivalent to $d/D = 0.6$, 1.1 and 1.6 , respectively. For each stage, a series of ten images, covering a footing displacement of $\sim 0.01D$ was analysed. Figures 10(b)–10(d) were combined to investigate the impact of the transition of deformation mechanisms from punch-through to meta-stable penetration on the bearing capacity factor.

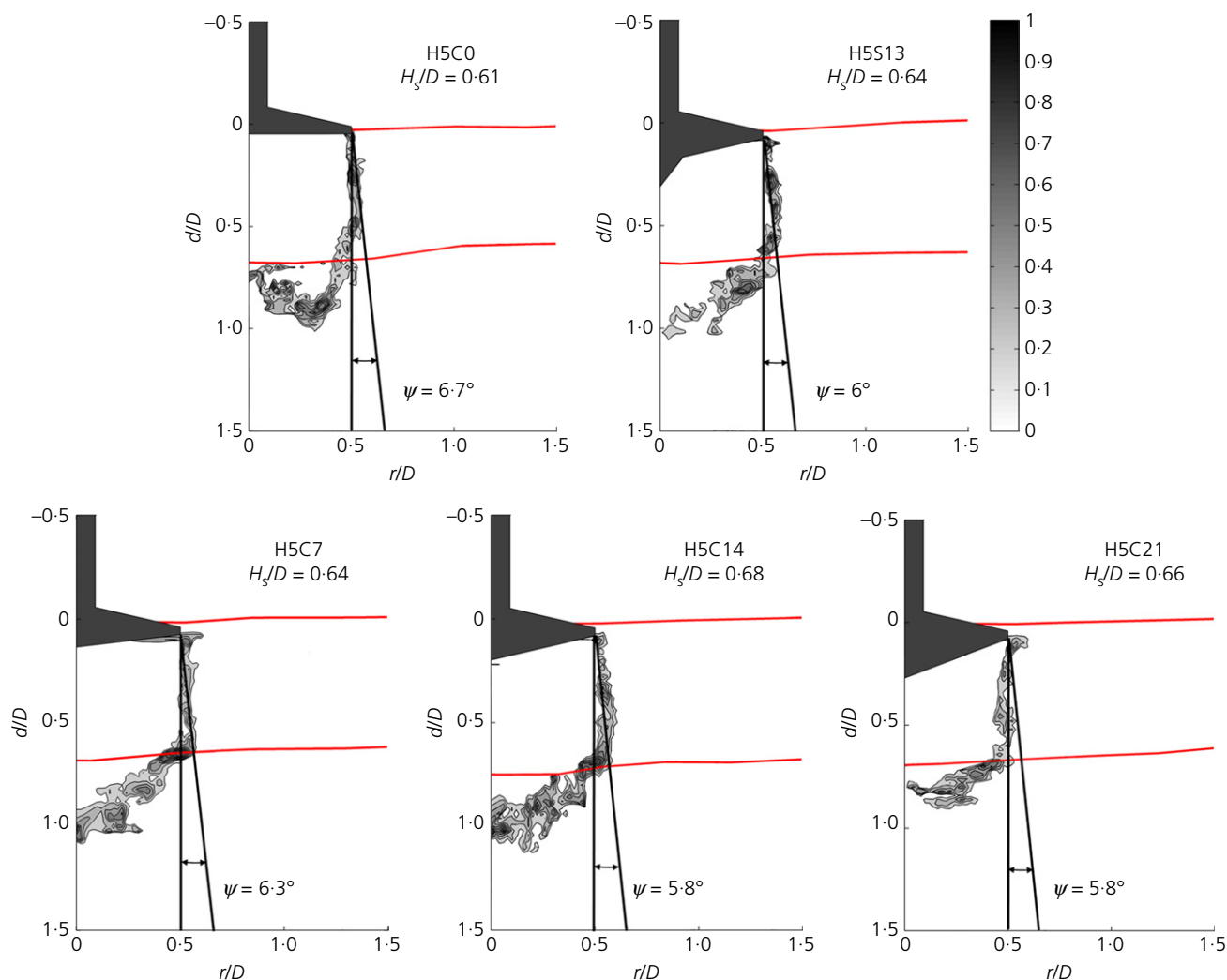


Figure 9. Normalised incremental deviatoric shear strain contours at q_{peak}

When the footing was penetrated to the original sand–clay interface (Figure 10(b)), a significant amount of sand beneath the footing is undergoing shearing, as the sand plug is not yet fully formed. The sand is shearing in a drained manner and is thus likely to be much stiffer and stronger than clay shearing in an undrained manner at a similar depth, due to the strength of sand being stress dependent in drained shear. Furthermore, a conical wedge of clay is trapped beneath the sand plug, enlarging the soil flow mechanism further. The combination of these factors causes the back-calculated bearing capacity factor to be greater than that estimated by Equation 7.

As the footing and sand plug penetrate to the depth of $d/D=1.1$, the back-calculated bearing capacity factor and

Equation 7 start to converge as less sand is now shearing at the periphery of the trapped sand plug (Figure 10(c)), although the trapped cone of clay beneath the sand plug is still evident. At a penetration depth of $d/D=1.6$ (Figure 10(d)), the soil flow mechanism consists of clay flowing around a composite foundation consisting of the footing and an entrapped meta-stable sand plug. The back-calculated bearing capacity factor response and Equation 7 converge as the shape of this composite foundation becomes meta-stable. Similar mechanistic behaviour was seen in other footing models of differing geometry, giving confidence that Equation 7 is generally applicable, so long as the depth when q_{peak} is equal to q_{clay} is greater than or equal to $1D$ below the sand–clay interface.

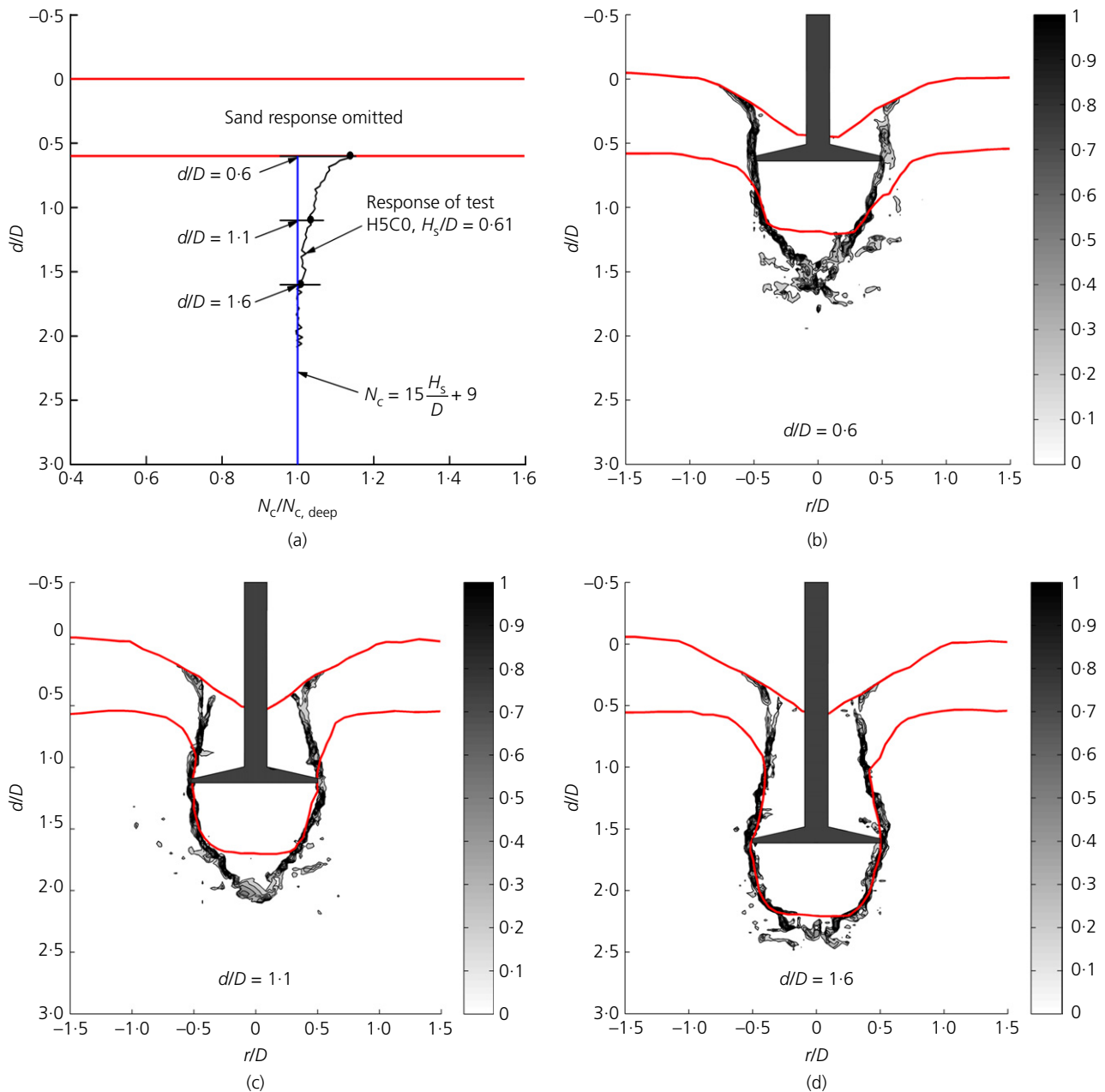


Figure 10. (a) Back-calculated bearing capacity factor and normalised incremental deviatoric shear strain distribution for test H5C0 at depths of (b) $0.6D$, (c) $1.1D$ and (d) $1.6D$

6.2 Trapped sand plug geometry

In Equation 6, the sand plug shape is idealised as a cylindrical plug. For footings with similar H_s/D but varying conical angle (ranging from 0° to 21°), the heights of the plugs, H_{plug} , were measured to account for the buoyancy effect when estimating the penetration resistance in the clay layer. Sand plug heights

were measured directly from the photographs recorded during penetration testing, with all measurements converted from pixels to model scale. Figure 11 presents the sand plug heights after $0D$, $0.5D$ and $1.0D$ penetration into the clay layer ($d/D = 0.6$, 1.1 and 1.6 , respectively), which facilitates investigation into potential differences in the evolution of sand plug height

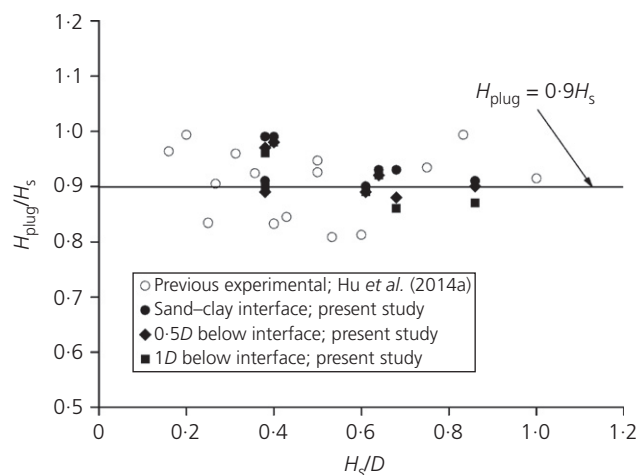


Figure 11. Normalised sand plug height at various penetration depths (note: previous experimental data are for 1D below interface)

with penetration depth for different footing shapes. The measurements of sand plug height from the centrifuge tests are presented alongside the experimental results (after 1.0D penetration into the clay layer) for footing S13 on medium dense sand (Hu *et al.*, 2014a) for comparison. Overall, seven tests in this study exhibit stable sand plug height throughout the footing penetration and reasonably fit the best-fit relationship of $H_{\text{plug}} = 0.9H_s$ resulting from previous analyses (Hu *et al.*, 2014b) on a spudcan with 13° underside. This suggests that the friction on the footing–sand interface underneath the footing is sufficient such that slippage cannot occur, irrespective of the inclination angle of the underside of the footing. Therefore, the sand plug height should be taken as a constant of $0.9H_s$ for simplicity, since no trend is evident in Figure 11 with respect to H_s/D or the conical angle of the underside of the footing.

6.3 Bearing capacity factor model

Centrifuge tests on punch through on sand overlying clay were collated from the literature, yielding a dataset that incorporated very dense ($I_D = 92\text{--}99\%$) and medium dense ($I_D = 43$ and 74%) sand centrifuge tests. Following the same method as described by Hu *et al.* (2014b), the N_c was derived at 1D below the sand–clay interface by applying Equation 6 to the testing data with the sand plug height taken as $0.9H_s$. Figure 12 presents the values of N_c that were back calculated from the experimental penetration resistance profiles. These N_c values are higher than the range of 9–14, typical for spudcan penetration in single clay layer with linearly increasing shear strength with depth (Hossain and Randolph, 2009; Houlsby and Martin, 2003). Larger sand layer height results in greater

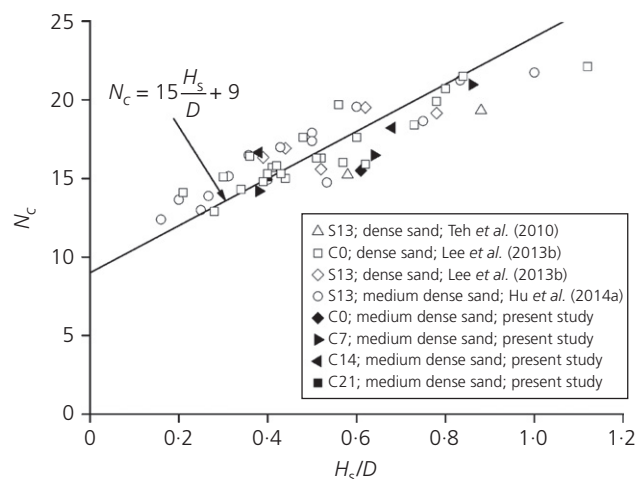


Figure 12. Bearing capacity factors from dense and medium dense sand centrifuge tests

sand plug height, enlarging the soil flow mechanism and increasing the bearing capacity factor, as is reflected in the form of Equation 7. Equation 7 was mainly derived from numerical analyses on loose and medium dense sand and only a single footing geometry, S13, was studied. Although the linear relationship from Equation 7 tends to underestimate N_c at smaller H_s/D and overestimate N_c at larger H_s/D moderately, the equation adequately estimates the bearing capacity factor of footing shapes ranging from flat to conical based with a conical angle in the range of 7–21° reasonably well. For footings with similar shape and H_s/D , the deep bearing capacity factor is not affected by the relative density of sand as once the sand plug is meta-stable the sand is not shearing as illustrated in Figure 10(d).

7. Conclusions

A series of model half-spudcan penetration tests have been reported that were conducted in the drum centrifuge. The effect of footing shape on penetration resistance and associated soil deformation mechanisms during punch through on sand overlying clay have been investigated. Photographs of soil flow mechanisms were captured in-flight and analysed using the PIV technique. Interpretation of this data has led to the following conclusions.

- The flat footing mobilised lower peak resistance than the footings with conical angle no less than 7°, which is in agreement with observations made in other series of centrifuge tests (e.g. Hu *et al.*, 2014a; Lee *et al.*, 2013a). There is no systematic difference in q_{peak} for footings with conical angle in the range of 7–21°.

- The back-calculated distribution factors, D_F were similar for footings with conical angles between 7° and 21° for similar H_s/D ratio. Larger conical angles result in increased accumulated radial strain near the outer radius of the footing. Higher stress on the failure surface in the sand layer is likely to be invoked and this in turn causes an increase in the D_F . However, proportionally higher accumulated deviatoric shear strains with increasing conical angle were also observed, causing significant softening of the sand in the same region and counteracting the effect of increased radial stress on the failure surface. This explains why the values of D_F for footings with conical angles in the range of 7 – 21° are located in a narrow range.
- Based on the back-calculated friction and dilation angles from a modified failure stress-dependent model, larger q_{peak} leads to lower values of ϕ' and ψ . This is consistent with the concept of gradual suppression of dilatancy under higher confining stress conditions during drained shearing. The normalised incremental deviatoric shear strain contours at q_{peak} validate the assumption in the failure stress-dependent model that the inclination angle of the trapped sand wedge may be taken as equal to the dilation angle of sand at peak resistance.
- The evolution of soil flow mechanisms after penetration of the composite foundation into the underlying clay layer was observed using PIV. The bearing capacity factor reduced gradually to a steady state at penetration depths $>0.5D$ from the sand–clay interface. A constant sand plug height of $0.9H_s$ was confirmed to be an adequate approximation.
- A linear equation can be used to estimate the bearing capacity factor of both spudcan and conical footings with conical angle $\leq 21^\circ$ reasonably well. The expression for bearing capacity is in a simple form, facilitating quick and easy evaluation of the potential for punch-through failure.

The conclusions provide further evidence of the benefit of incorporating the properties of sand into the analytical model of Hu *et al.* (2014a) and Lee *et al.* (2013b), when compared with the methods currently provided to engineers in the ISO site-specific assessment of jack-up unit guideline (ISO, 2012).

Acknowledgements

This work forms part of the activities of the Centre for Offshore Foundation Systems (COFS), which is supported by the Lloyd's Register Foundation as a Centre of Excellence and now forms one of the primary nodes of the Australian Research Council (ARC) Centre of Excellence for Geotechnical Science and Engineering. Lloyd's Register Foundation invests in science, engineering and technology for public benefit, worldwide. This project has received additional support from the Australia–China Natural Gas Technological

Partnership Fund and the ARC Discovery program (DP1096764). The authors are grateful for this support and also to drum centrifuge technicians Mr Bart Thompson and Mr Gregory Outridge for their assistance during the experimental work.

REFERENCES

- Acosta-Martinez HE and Gourvenec S (2006) *One-Dimensional Consolidation Tests on Kaolin Clay*. University of Western Australia, Geomechanics Group, Perth, Australia, Research Report GEO: 06385.
- Bolton MD (1986) The strength and dilatancy of sands. *Géotechnique* **36**(1): 65–78, <http://dx.doi.org/10.1680/geot.1986.36.1.65>.
- Cassidy MJ (2012) Experimental observation of the penetration of spudcan footings in silt. *Géotechnique* **62**(8): 727–732, <http://dx.doi.org/10.1680/geot.9.T.020>.
- Cassidy MJ, Quah CK and Foo KS (2009) Experimental investigation of the reinstallation of spudcan footings close to existing footprints. *Journal of Geotechnical and Geoenvironmental Engineering* **135**(4): 474–486.
- Cheong J (2002) *Physical Testing of Jack-Up Footings on Sand Subjected to Torsion*. Honours thesis, University of Western Australia, Perth, Australia.
- Chung SF, Randolph MF and Schneider JA (2006) Effect of penetration rate on penetrometer resistance. *Journal of Geotechnical and Geoenvironmental Engineering* **132**(9): 1188–1196.
- Craig WH and Chua K (1990) Deep penetration of spud-can foundation on sand and clay. *Géotechnique* **40**(4): 541–556, <http://dx.doi.org/10.1680/geot.1990.40.4.541>.
- Dean ETR (2010) *Offshore Geotechnical Engineering – Principles and Practice*. Thomas Telford, Reston, VA, USA, 520p.
- Drescher A and Detournay E (1993) Limit load in translational failure mechanics for associative and non-associative materials. *Géotechnique* **43**(3): 443–456, <http://dx.doi.org/10.1680/geot.1993.43.3.443>.
- Hossain MS and Randolph MF (2009) New mechanism-based design approach for spudcan foundations on single layer clay. *Journal of Geotechnical and Geoenvironmental Engineering* **135**(9): 1264–1274.
- Hossain MS, Randolph MF, Hu Y and White DJ (2006) Cavity stability and bearing capacity of spudcan foundations on clay. *Proceedings of Offshore Technology Conference, Houston, TX, USA*, OTC 17770.
- Houlsby GT and Martin CM (2003) Undrained bearing capacity factors for conical footings on clay. *Géotechnique* **53**(3): 513–520, <http://dx.doi.org/10.1680/geot.2003.53.5.513>.
- Hu P (2015) *Predicting Punch-Through Failure of a Spudcan on Sand Overlying Clay*. PhD thesis, University of Western Australia, Perth, Australia.

- Hu P, Stanier SA, Cassidy MJ and Wang D (2014a) Predicting peak resistance of spudcan penetrating sand overlying clay. *Journal of Geotechnical and Geoenvironmental Engineering* **140**(2): 04013009.
- Hu P, Wang D, Cassidy MJ and Stanier SA (2014b) Predicting the resistance profile of a spudcan penetrating sand overlying clay. *Canadian Geotechnical Journal* **51**(10): 1151–1164.
- ISO (International Organization for Standardization) (2012) *Petroleum and Natural Gas Industries – Site-Specific Assessment of Mobile Offshore Unit – Part 1: Jack-Ups*. ISO, Geneva, Switzerland, ISO/FDIS 19905-1.
- Lee KK, Cassidy MJ and Randolph MF (2013a) Bearing capacity on sand overlying clay soils: experimental and finite element investigation of potential punch-through failure. *Géotechnique* **63**(15): 1271–1284, <http://dx.doi.org/10.1680/geot.12.P.175>.
- Lee KK, Randolph MF and Cassidy MJ (2013b) Bearing capacity on sand overlying clay soils: a simplified conceptual model. *Géotechnique* **63**(15): 1285–1297, <http://dx.doi.org/10.1680/geot.12.P.176>.
- Menzies D and Roper R (2008) Comparison of jack-up rig spudcan penetration methods in clay. *Proceedings of Offshore Technology Conference, Houston, TX, USA*, OTC 19545.
- Muir Wood D (2012) Heterogeneity and soil element testing. *Geotechnique Letters* **2**(3): 101–106, <http://dx.doi.org/10.1680/geolett.12.00019>.
- Osborne JJ, Houlsby GT, Teh KL et al. (2009) Improved guidances of the prediction of geotechnical performance of spudcan foundations during installation and removal of jack-up units. *Proceedings of Offshore Technology Conference, Houston, TX, USA*, OTC 20291.
- Stanier SA and White DJ (2013) Improved image-based deformation measurement in the centrifuge environment. *Geotechnical Testing Journal* **36**(6): 1–14.
- Stanier SA, Ragni R, Bienen B and Cassidy MJ (2014) Observing the effects of sustained loading on spudcan footings in clay. *Géotechnique* **64**(11): 918–926, <http://dx.doi.org/10.1680/geot.14.P.003>.
- Stewart DP and Randolph MF (1991) A new site investigation tool for the centrifuge. *Proceedings of International Conference on Centrifuge Modelling – Centrifuge'91*, Boulder, USA, pp. 531–538.
- Teh KL (2007) *Punch-Through of Spudcan Foundation in Sand Overlying Clay*. PhD thesis, National University of Singapore, Singapore.
- Teh KL, Cassidy MJ, Leung CF et al. (2008) Revealing the bearing capacity mechanisms of a penetrating spudcan through sand overlying clay. *Géotechnique* **58**(10): 793–804, <http://dx.doi.org/10.1680/geot.2008.58.10.793>.
- Teh KL, Leung CF, Chow YK and Cassidy MJ (2010) Centrifuge model study of spudcan penetration in sand overlying clay. *Géotechnique* **60**(11): 825–842, <http://dx.doi.org/10.1680/geot.8.P.077>.
- Ullah SN and Hu Y (2012) A numerical investigation into the bottom boundary effect for spudcan penetration on sand overlying clay in centrifuge test. *Proceedings of 31st International Conference on Ocean, Offshore and Arctic Engineering, OMAE 2012-84246*, Rio De Janeiro, Brazil, pp. 229–237.
- White DJ and Bolton MD (2004) Displacement and strain paths during plane-strain model pile installation in sand. *Géotechnique* **54**(6): 375–397, <http://dx.doi.org/10.1680/geot.2004.54.6.375>.
- White DJ, Take WA and Bolton MD (2003) Soil deformation measurement using particle image velocimetry (PIV) and photogrammetry. *Géotechnique* **53**(7): 619–631, <http://dx.doi.org/10.1680/geot.2003.53.7.619>.

HOW CAN YOU CONTRIBUTE?

To discuss this paper, please email up to 500 words to the editor at journals@ice.org.uk. Your contribution will be forwarded to the author(s) for a reply and, if considered appropriate by the editorial board, it will be published as discussion in a future issue of the journal.

International Journal of Physical Modelling in Geotechnics relies entirely on contributions from the civil engineering profession (and allied disciplines). Information about how to submit your paper online is available at www.icevirtuallibrary.com/page/authors, where you will also find detailed author guidelines.